

Supporting Information

Enhanced Oxygen Activation on Atomically Dispersed Au Catalyst with Dual Active Sites for Room-Temperature Formaldehyde Oxidation

Huixia Li,^a Shaofan Fang,^b Guimin Jiang,^a Zuotai Zhang*,^a

^aSchool of Environmental Science and Engineering, Guangdong Provincial Key Laboratory of Soil and Ground water Pollution Control, Southern University of Science and Technology, Shenzhen 518055, People's Republic of China.

^bInternational Collaborative Laboratory of 2D Materials for Optoelectronics Science and Technology of Ministry of Education, Institute of Microscale Optoelectronics, Shenzhen University, Shenzhen 518060, P. R. China.

Table of contents

Details	Page No.
Experimental Section	4-8
Fig. S1. Scanning electron micrographs of the CeO ₂ nanorod supports of Au/CeO ₂ , Au/CeO ₂ -350, Au/CeO ₂ -550 and Au/CeO ₂ -750 catalysts, respectively.	9
Fig. S2. Structures and morphologies of CeO ₂ supports and exposed facets. (a, b, c, d) Low-magnification TEM images of Au/CeO ₂ , Au/CeO ₂ -350, Au/CeO ₂ -550 and Au/CeO ₂ -750 catalysts. (a1, b1, c1, d1) HRTEM images of CeO ₂ -rod supports of Au/CeO ₂ , Au/CeO ₂ -350, Au/CeO ₂ -550 and Au/CeO ₂ -750, respectively. (e) HAADF-STEM of Au/CeO ₂ -550 with element distribution images (f–h) corresponding to Au, Ce, and O.	10
Fig.S3. TEM images of (a, a1) Au/CeO ₂ , (b, b1)Au/CeO ₂ -350, (c,c1)Au/CeO ₂ -750, and (a2, b2, c2) the corresponding particle size distribution images.	11
Fig. S4 HRTEM images of Au ₃ O ₂ nanoparticle for Au/CeO ₂ -750, The EDS spectrum of Au ₃ O ₂ nanoparticle is inserted in the image.	12
Fig. S5 O ₂ -TPD-MS profiles of the Au/CeO ₂ -550 catalyst.	13
Fig. S6. (a) N ₂ adsorption–desorption isotherms and (b) pore size distributions of Au/CeO ₂ , Au/CeO ₂ -350, Au/CeO ₂ -550 and Au/CeO ₂ -750 catalysts.	14
Fig. S7. HCHO conversion of the contrast samples CeO ₂ .	15
Fig. S8 Time-resolved DRIFTS results for catalyst samples obtained using CO as a probe molecule: (a) Au/CeO ₂ -350, (b) Au/CeO ₂ -550, and temporal changes in peak intensities of (c) Au ^{δ+} -CO and (d) Au ⁰ -CO species.	16

Fig. S9. The XRD patterns of all catalysts after the HCHO oxidation reaction.	17
Fig. S10 Stability of Au/CeO ₂ -550 in HCHO oxidation at 30 °C under dry reaction conditions.	18
Fig. S11. In situ DRIFT spectra of CeO ₂ as a function of temperature under operando HCHO oxidation conditions in different wavenumber regions.	19
Fig. S12 DRIFT spectra of (a) Au/CeO ₂ , (b) Au/CeO ₂ -350 and (c) Au/CeO ₂ -750 catalysts as a function of temperature under operando HCHO oxidation conditions in different wavenumber regions and the expanded regions of the In situ DRIFTS patterns in the range of 2500–2200 cm ⁻¹ .	20
Fig. S13 DRIFTS record the dynamic changes of (a) adsorbed intermediates and (b) carbon dioxide on Au/CeO ₂ -550 catalysts in the HCHO, He and O ₂ gas flow at room temperature.	21
Table S1. Particulate properties of the given catalysts.	22
Table S2. Reducibility of all the given catalysts obtained by H ₂ -TPR.	23
Table S3. Comparison of catalytic performance in HCHO oxidation over Au/CeO ₂ -550 and those catalysts reported in literature.	24
Reference	25-26

Experimental Section

All chemicals and solvents were of reagent grade and used without further purification.

Catalyst preparation

Synthesis of CeO₂ nanorods

All the chemical reagents used in our experiments were of analytical grade and used as purchased without further purification. Synthesis of the CeO₂ nanorods was performed via a hydrothermal method. Typically, 4 mmol Ce(NO₃)₃·6H₂O (99%, Sigma Aldrich) and 0.48 mol NaOH (96%, Aladdin) were dissolved in 10 mL and 70 mL of deionized water, respectively. Then the Ce(NO₃)₃·6H₂O solution was added dropwise into the NaOH solution under vigorous magnetic stirring at room temperature for 30 min. The as-obtained light purple slurry was then transferred into a 100 mL Teflon-lined autoclave and hydrothermally heated at 120 °C for 24 h. After cooling to room temperature, the precipitates were filtered and washed using the deionized water, before being dried at 80 °C for 24 h to obtain the final CeO₂ nanorods product.

Synthesis of Au supported CeO₂ nanorods

Gold species (2 wt% Au) were loaded onto the CeO₂ nanorods via a wet impregnation process in HAuCl₄ aqueous solutions (1 mg/mL) that lasted for approximately 30 min, immediately after, the 0.2 M NaOH solution was injected into the above suspension. After stirring for 2 h at 60 °C, the powder was collected after filtered and washing several times with deionized water to remove unreacted HAuCl₄ and unloaded Au nanoparticles, and subsequently dried at 80 °C. The obtained sample is referred to hereinafter as Au/CeO₂. Some of the Au/CeO₂ samples were then calcined in air at 350 °C, 550 °C and 750 °C, respectively. Meanwhile, these samples were denoted as Au/CeO₂-350, Au/CeO₂-550, and Au/CeO₂-750, respectively.

Sample characterization

Chemical compositions of samples were analyzed using inductively coupled plasma-optical emission spectroscopy (ICP-MS, Agilent 7500x, USA). Nitrogen adsorption isotherms and pore distributions of the samples were measured using an asap2020 analyzer (Micromeritics Instrument Corporation, USA). Specific surface areas of the samples were calculated from the linear portion of the adsorption branch of the isotherms. Pore size and pore volume analysis of samples were carried out with Barrett–Joyner–Halenda (BJH) method using desorption branch of the isotherms. Powder X-ray diffraction (XRD) pattern were acquired using a Rigaku Smart Lab X-ray diffractometer equipped with a Cu-K α radiation ($\lambda=0.15418$ nm) at 45 kV and 45 mA in the range of 2θ from 10° to 80°. Temperature programmed techniques (TPR) and temperature programmed desorption (TPD) profiles of the samples (~30mg) were obtain by Micromeritics AutoChem II 2920 equipped with Thermal Conductivity Detector (TCD). Raman Spectroscopy experiments were performed on a Horiba Scientific Lab RAMHR Evolution instrument (Horiba Scientific, Japan) in confocal imaging mode with a 50 \times microscope objective and a 532 nm solid-state laser as an excitation source. X-ray Photoelectron Spectroscopy (XPS) experiments were conducted in a K-Alpha+ Thermo fisher 250i spectrometer (Thermo Scientific, USA), equipped with a monochromatic Al K α X-ray source (1486.6 eV). All spectra were calibrated using the C 1s peak at 284.8 eV. Microscopic structure analyses were undertaken using scanning electron microscopy (SEM, J SU 8020) and (TEM, Tecnai G2 S-Twin F20, FEI, USA).

An O₂-TPD experiment was performed on AutoChem II 2920, the sample (30 mg) was first treated under He at 300 °C for 1h. After the temperature was slowly cooled down to 50 °C, followed by a 10% O₂/He (40 mL/min) for 1h, then He flow (40 mL/min) was switched to purge

for 1h to remove the weak physical adsorption O₂ on the sample surface. Finally, the sample was heated from 50 to 800 °C at 10 °C/min. O₂-TPD quadruple mass spectroscopy (Q-MS) was used to analyze evolving gases. The signals for O₂ (m/z = 32), CO₂ (m/z = 44), CO (m/z = 28) and H₂ (m/z = 2) were monitored by using a Bel Mass bench top gas analysis system connected to an AutoChem II 2920 outlet.

In situ diffuse reflectance Fourier transform infrared spectroscopy (DRIFTS) was performed on a Nicolet iS50 spectrometer, equipped with a liquid N₂ cooled MCT detector. The spectra of samples were recorded using a Nicolet iS50 FT-IR spectrometer (Thermo Scientific, USA) equipped with Harrick DRIFTS accessory and Harrick high temperature reaction chamber (Harrick Scientific Products, Inc., USA). Prior to the measurement, the catalysts (about 2 mg) were treated in-situ at 200 °C with flow of pure N₂ (flow rate, 40 mL·min⁻¹) to remove the surface contaminants. A background spectrum was collected for correction after cooling to 30 °C. Then, the reaction gas (10 mL of 220 ppm HCHO and 20 mL of 20% O₂/Ar), was introduced into the in-situ chamber at a flow rate of 10 mL·min⁻¹. The spectra were averaged over 48 scans with a resolution of 4 cm⁻¹.

CO probe molecule experiment: An injection of 5% CO/Ar gas into the reaction chamber ensured that saturated CO adsorption was achieved for each sample, and the subsequent injection of Ar gas ensured that the residual CO gas was removed; DRIFTS was performed at regular time intervals after the CO/Ar gas injection.

Catalytic activity test of the HCHO oxidation

Catalytic activity of the as-prepared catalysts was measured in a feed reactor. The catalyst (50 mg) was loaded between quartz wool layers in a tube reactor. The feed contained 220 ppm

gaseous HCHO, which was introduced into the reactor by flowing Ar (10 mL/min) over paraformaldehyde (99%, Aldrich) in a thermostatic bath (36 °C) and 20% O₂/Ar (20 mL/min) at a rate of $1 \times 10^3 \text{ cm}^3 \cdot \text{min}^{-1} \cdot \text{g}^{-1}$ (roughly 36000 mL·g⁻¹·h⁻¹ GHSV). The conversion of HCHO was analyzed using an online gas chromatograph equipped with a hydrogen flame ionization detector (FID) and Ni catalyst convertor which was used to convert carbon oxides quantitatively into methane before the detector. To avoid interfering gas adsorption effects, the test data were collected after the reactions had reached stable states. No other carbonaceous compounds except CO₂ were detected in the products in all cases.

HCHO conversion was calculated as follows:

$$X_{HCHO}(\%) = \frac{F_{HCHO}^{in} - F_{HCHO}^{out}}{F_{HCHO}^{in}} \times 100$$

Where X represents percentage conversion and F is the molar flow of the indicated gas (inlet or outlet).

Next, we carried out kinetic measurements to study the intrinsic activities of the Au/CeO₂, Au/CeO₂-350, Au/CeO₂-550 and Au/CeO₂-750 catalysts. The catalyst (10 mg) was heated in a gas flow of 150 mL/min (WHSV: 900,000 mL·g⁻¹·h⁻¹), which contains 220 ppm HCHO/13 vol% O₂/Ar. Kinetics data were collected at the HCHO conversion below 20%.

For HCHO oxidation reaction, the reaction rates were calculated based on the following equations,

$$r = \frac{C_{HCHO} \cdot X_{HCHO} \cdot V \cdot P_{atm}}{m_{cat} \cdot R \cdot T} (\text{mol} \cdot \text{s}^{-1} \cdot \text{g}_{cat}^{-1})$$

where r is the reaction rate of the catalysts (mol·s⁻¹·g_{cat}⁻¹), m_{cat} is the mass of the Au catalyst (g); R is the molar gas constant (Pa·m³·mol⁻¹·K⁻¹), T is the temperature (K), C_{HCHO} is the

concentration of HCHO (%), X_{HCHO} is the percentages of HCHO conversion (%), V is the flow rate ($\text{m}^3 \cdot \text{s}^{-1}$), and P_{atm} is the atmospheric pressure (Pa).

The apparent activation energy was calculated based on the Arrhenius equation as given below,

$$r = r_0 e^{-E_a/RT}$$

where E_a represents the energy barrier (activation energy), which can be obtained from the slope of a plot of $-\ln(r)$ versus $1/T$, and r_0 is a constant.

The turnover frequency (TOF) values were calculated as follows.

$$TOFs (s^{-1}) = \frac{X_{\text{HCHO}} \times 1\% \times V(\text{cm}^3 \cdot \text{min}^{-1}) \times M(\text{catalyst})}{R_g \times 60 \times 1000 \times m(\text{g})}$$

Where V is the total gas flow, R_g is the molar volume of gas ($22.4 \text{ L} \cdot \text{mol}^{-1}$), m is the mass of Au in the catalyst, and M is the molecular mass of Au ($196.97 \text{ g} \cdot \text{mol}^{-1}$).

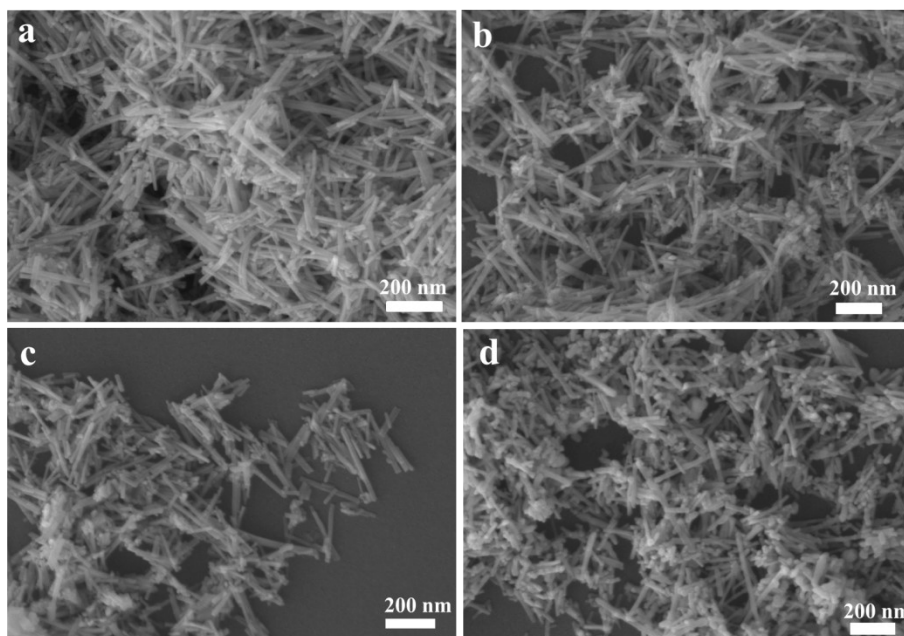


Fig. S1 Scanning electron micrographs of the CeO₂ nanorod supports of Au/CeO₂, Au/CeO₂-350, Au/CeO₂-550 and Au/CeO₂-750 catalysts, respectively.

SEM images of the catalysts are shown in Fig. S1. All the given catalysts exhibited the similar nanorod morphology. The CeO₂ nanorod support in Au/CeO₂-750 exhibited a slight agglomeration compared with other CeO₂ nanorod supports.

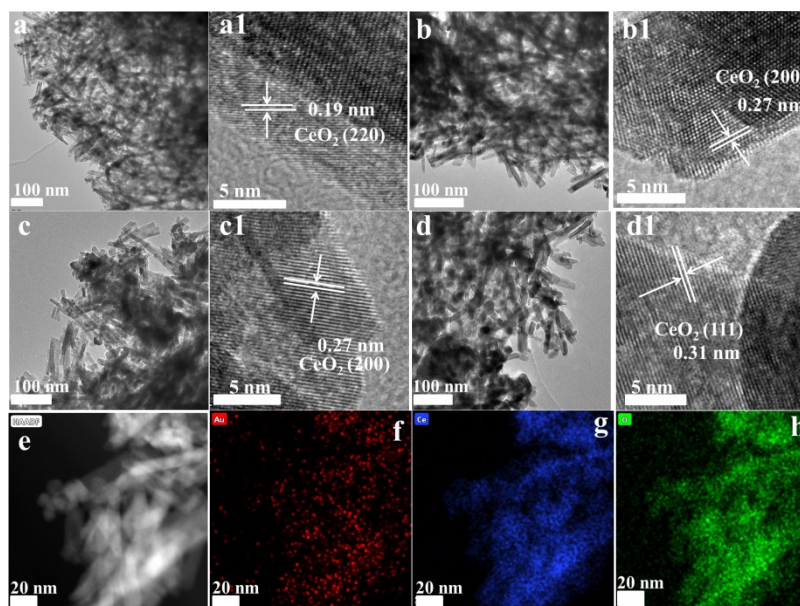


Fig. S2 Structures and morphologies of CeO_2 supports and exposed facets. (a, b, c, d) Low-magnification TEM images of Au/CeO_2 , $\text{Au/CeO}_2\text{-350}$, $\text{Au/CeO}_2\text{-550}$ and $\text{Au/CeO}_2\text{-750}$ catalysts. (a1, b1, c1, d1) HRTEM images of CeO_2 -rod supports of Au/CeO_2 , $\text{Au/CeO}_2\text{-350}$, $\text{Au/CeO}_2\text{-550}$ and $\text{Au/CeO}_2\text{-750}$, respectively. (e) HAADF-STEM of $\text{Au/CeO}_2\text{-550}$ with element distribution images (f–h) corresponding to Au, Ce, and O.

The SEM (Fig. S1) and TEM (Fig. S2) images show that the target CeO_2 nanorod supports are successfully synthesized by the adopted hydrothermal methods. The HRTEM image (Fig. S2a1) shows a distinct (220) lattice fringe with an interplanar spacing of 0.19 nm of Au/CeO_2 catalyst. The CeO_2 nanorod support of $\text{Au/CeO}_2\text{-350}$ also show that the determined d-spacing derived from the HRTEM analysis of 0.27 nm is consistent with the layer spacing in (200) orientation (Fig. S2b1). Fig. S2d represents the similar CeO_2 nanorod morphology of $\text{Au/CeO}_2\text{-750}$. The HRTEM image of the CeO_2 nanorods show the clear interplanar spacing of 0.31 nm, corresponding to the (111) lattice fringes of CeO_2 .

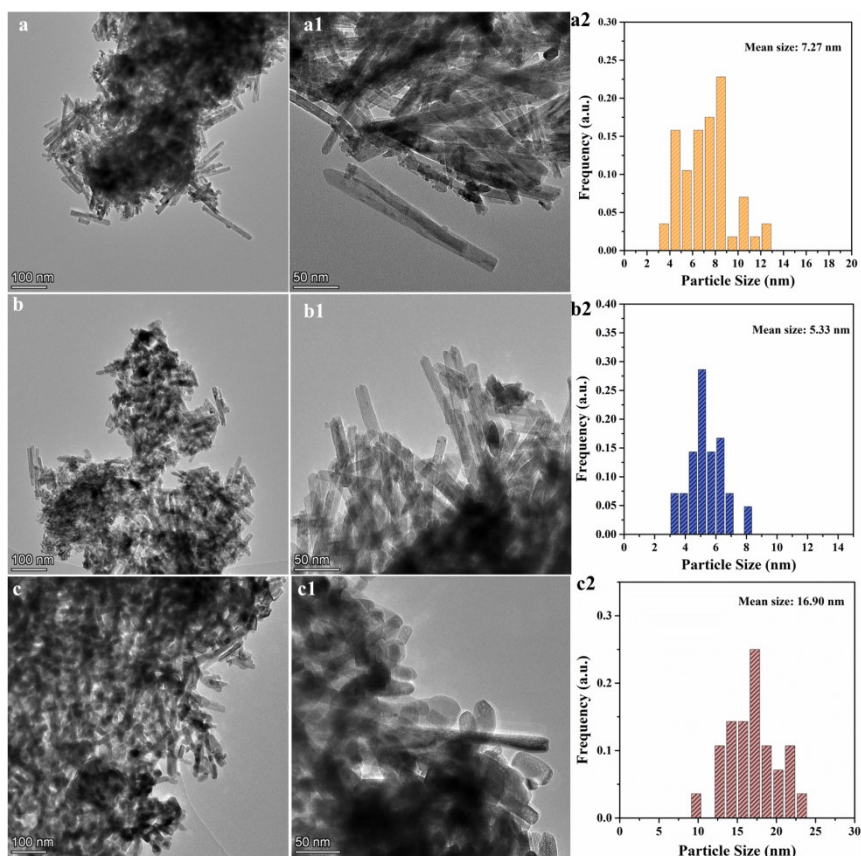


Fig. S3 TEM images of (a, a1) Au/CeO₂, (b, b1) Au/CeO₂-350, (c, c1) Au/CeO₂-750, and (a2, b2, c2) the corresponding particle size distribution images.

The Au mean particle size distribution for Au/CeO₂, Au/CeO₂-350 and Au/CeO₂-750 are about 7.27 nm, 5.33 nm and 16.90 nm, respectively. The particle size distribution region of Au/CeO₂-350 catalyst is between that of Au/CeO₂ and Au/CeO₂-750. As shown in Fig. S3a, a1, b, b1, Au nanoparticles with an average size of approximately 7.27 nm and 5.33 nm are observed for the Au/CeO₂ and Au/CeO₂-350 catalysts, respectively. As shown in Fig. S2c, c1, Au NPs with the average size of 16.90 nm are observed on the CeO₂ nanorods surface for the Au/CeO₂-750 catalyst.

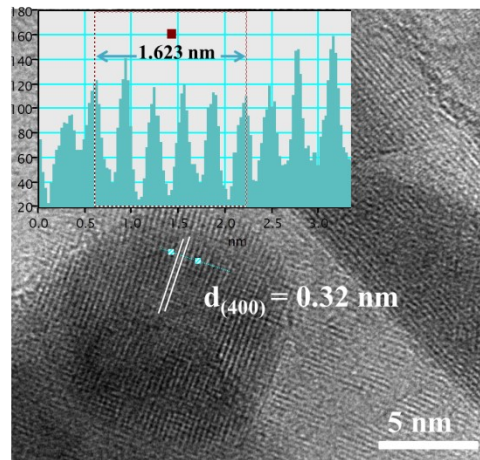


Fig. S4 HRTEM images of Au_3O_2 nanoparticle for Au/CeO_2 -750, The EDS spectrum of Au_3O_2 nanoparticle is inserted in the image.

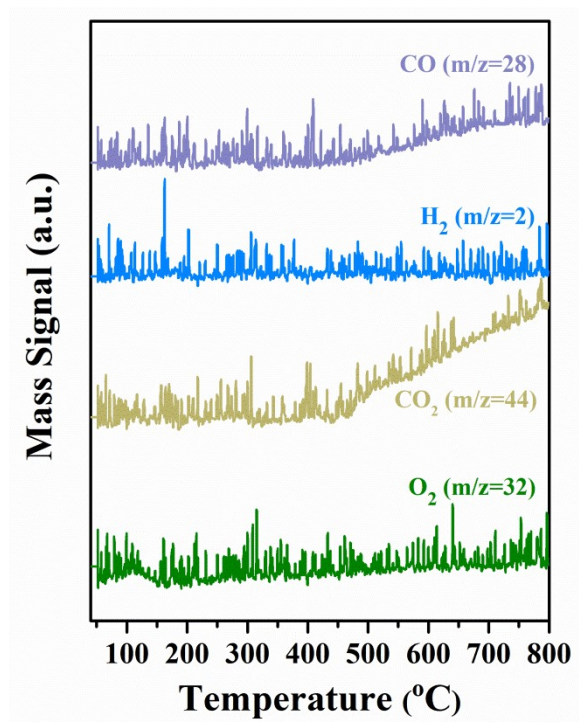


Fig. S5 O₂-TPD-MS profiles of the Au/CeO₂-550 catalyst.

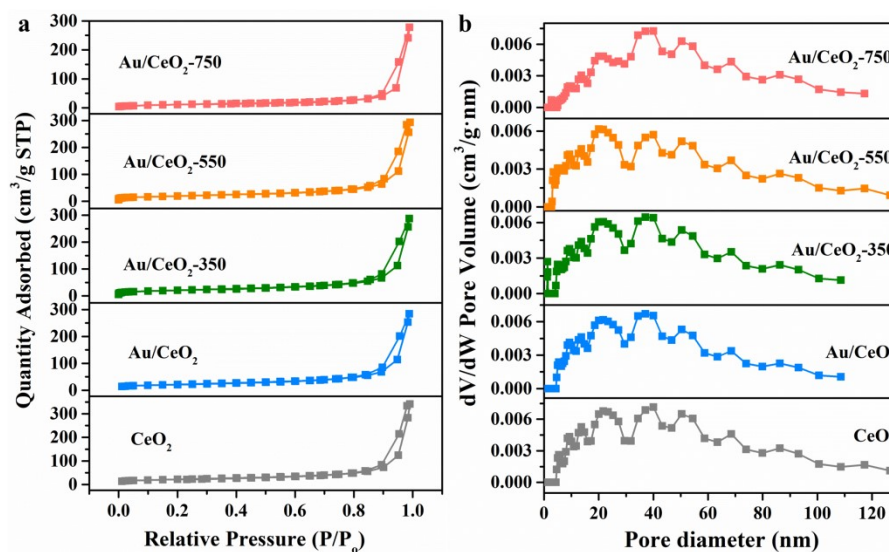


Fig. S6 (a) N_2 adsorption–desorption isotherms and (b) pore size distributions of Au/CeO_2 , Au/CeO_2 -350, Au/CeO_2 -550 and Au/CeO_2 -750 catalysts.

To assess the porosity of all the catalysts, N_2 adsorption–desorption measurements were conducted. All samples gave a typical Type-IV isotherm with H3-type hysteresis loops over the relative pressure range, $P/P_0 = 0.9$ -1 (Fig. S6a), indicating a mesoporous feature according to the IUPAC classification.^{1, 2, 3} No nitrogen adsorptions observed in lower relative pressure ($P/P_0 = 0$ -0.9) demonstrate the absence of micropores for our samples. BJH pore size distribution curves for the samples also confirmed their mesopore feature, showing a broad pore size distribution from 2 to 80 nm (Fig. S6b). BET surface areas for samples CeO_2 , Au/CeO_2 , Au/CeO_2 -350, Au/CeO_2 -550 and Au/CeO_2 -750 were 76.46, 75.65, 72.05, 67.72 and 43.63 m^2/g , respectively (Table S2). The surface area gradually decreases with the calcination temperature increasing. The overall textural properties are listed in Table S1.

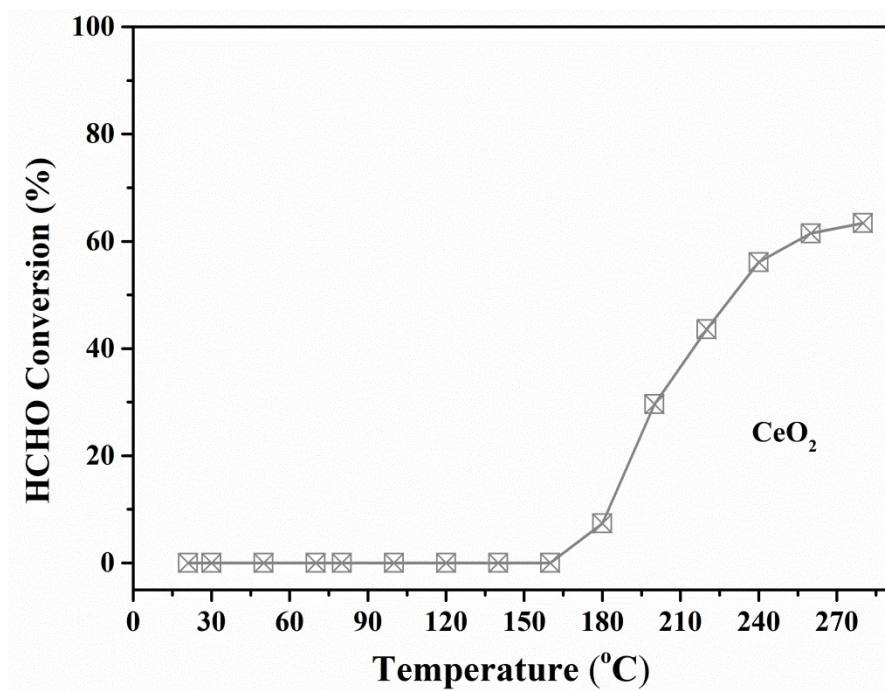


Fig. S7 HCHO conversion of the contrast samples CeO₂.

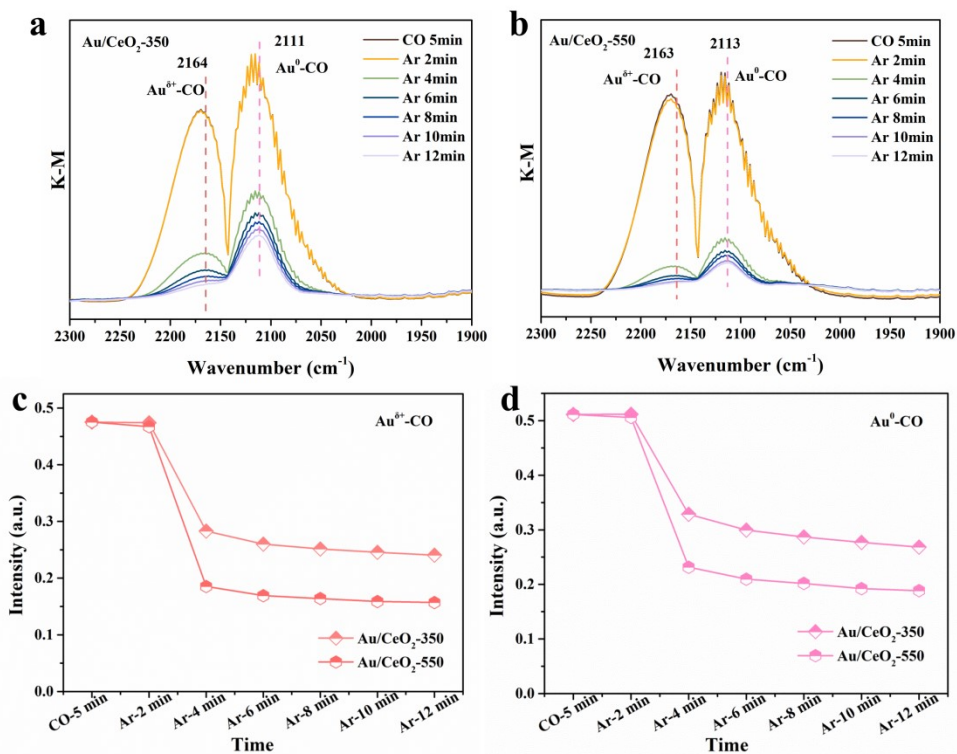


Fig. S8 Time-resolved DRIFTS results for catalyst samples obtained using CO as a probe molecule: (a) Au/CeO₂-350, (b) Au/CeO₂-550, and temporal changes in peak intensities of (c) Au^{δ+}-CO and (d) Au⁰-CO species.

The CO was regarded as the probe molecule to detect desorption capacities of Au/CeO₂-350 and Au/CeO₂-550 via in situ DRIFTS. In a typical IR spectrum of CO, the adsorption band at 2161–2166 cm⁻¹ was assigned to Au^{δ+}-CO ($1 \leq \delta \leq 3$).⁴⁻⁶ In addition, it was observed that the CO molecules adsorbed on the metallic Au nanoparticles (Au⁰-CO) generated the 2103–2113 cm⁻¹ band in the spectra of the catalysts.^{7,8} Comparing the intensity of CO desorption during Ar purging (Fig. S7c, d), the Au⁰-CO and Au^{δ+}-CO bands of the Au/CeO₂-350 catalyst indicated that the adsorbed CO was lost much more slowly compared to the Au/CeO₂-550 catalyst. Thus, the Au/CeO₂-350 catalyst possesses the weak gas-desorption capacity.

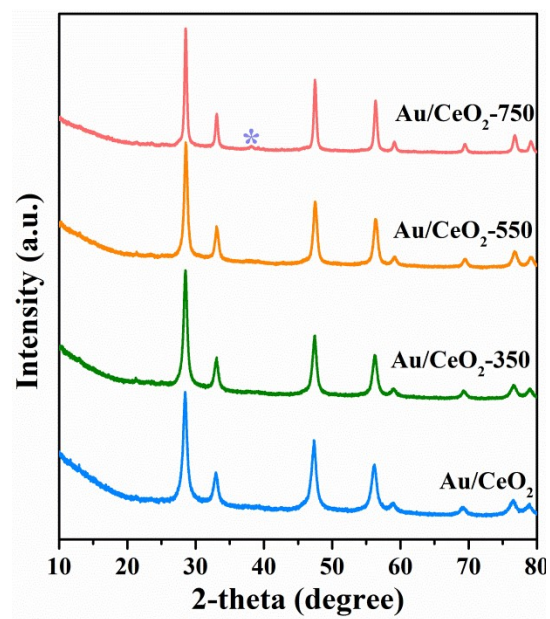


Fig. S9 XRD patterns of all catalysts after the HCHO oxidation reaction.

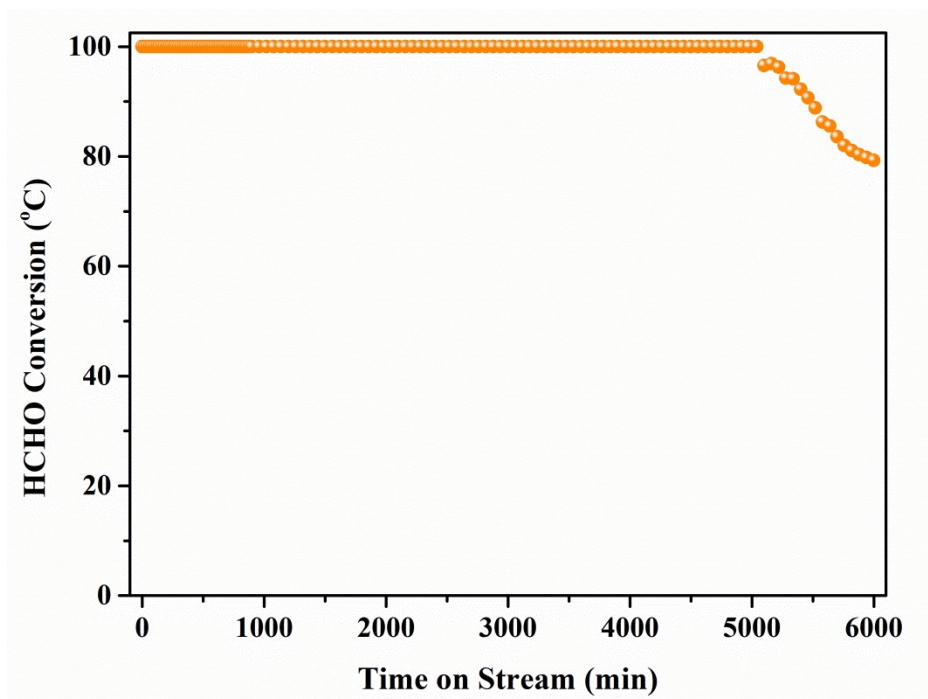


Fig. S10 Stability of Au/CeO₂-550 in HCHO oxidation at 30 °C under HCHO oxidation reaction conditions.

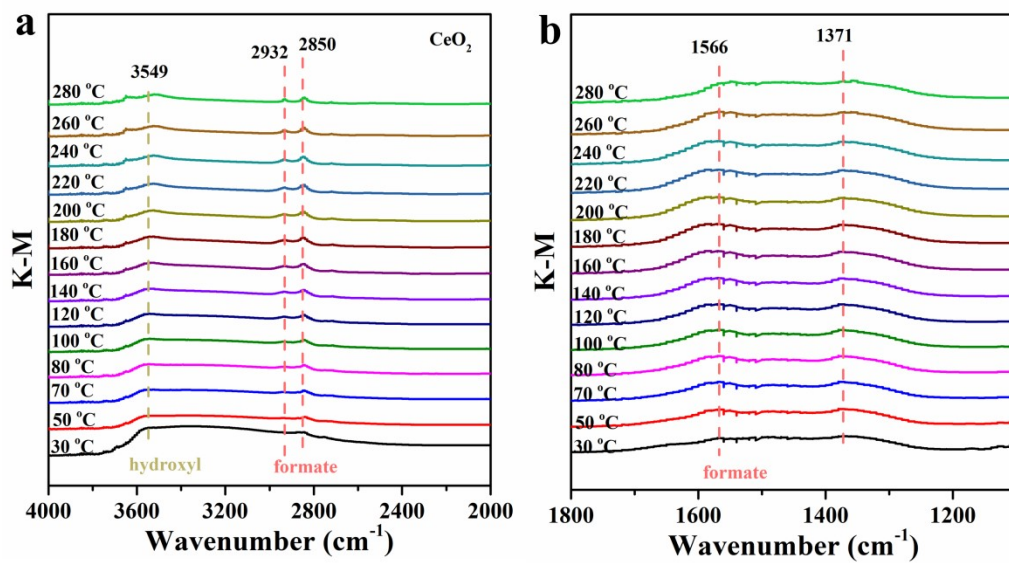


Fig. S11 In situ DRIFT spectra of CeO₂ as a function of temperature under operando HCHO

oxidation conditions in different wavenumber regions.

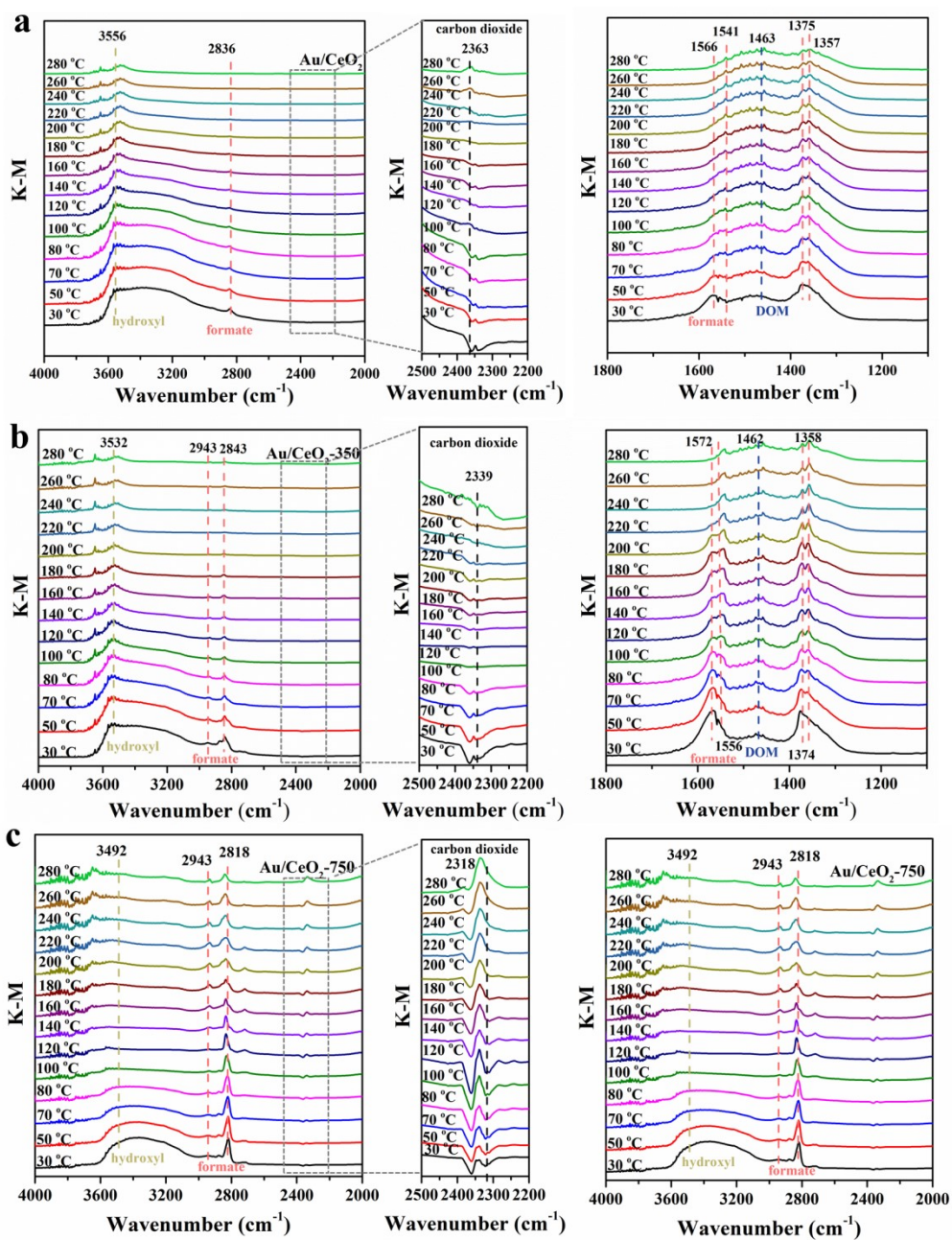


Fig. S12 DRIFT spectra of (a) Au/CeO₂, (b) Au/CeO₂-350 and (c) Au/CeO₂-750 catalysts as a function of temperature under operando HCHO oxidation conditions in different wavenumber regions and the expanded regions of the In situ DRIFTS patterns in the range of 2500–2200 cm⁻¹.

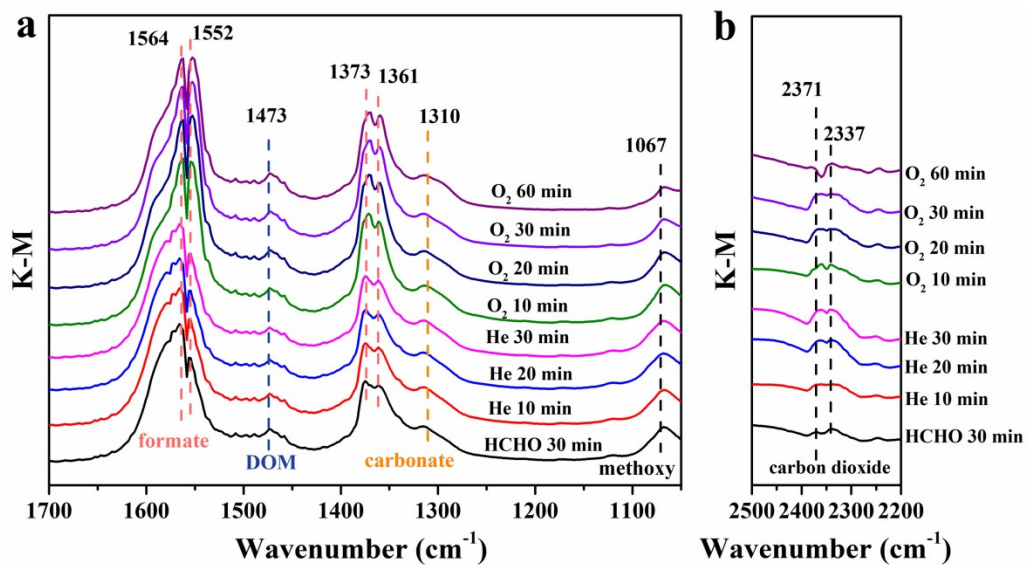


Fig. S13 DRIFTS record the dynamic changes of (a) adsorbed intermediates and (b) carbon dioxide on Au/CeO₂-550 catalysts in the HCHO, He and O₂ gas flow at room temperature.

Table S1. Particulate properties of the given catalysts.

Samples	Surface	Pore volume	Pore diameter (nm)	Au loading (%)^a
	area	(cm³/g)		
	(m²/g)			
CeO₂	76.46	0.53	27.50	0
Au/CeO₂	75.65	0.44	23.37	2.62
Au/CeO₂-350	72.05	0.44	23.11	3.14
Au/CeO₂-550	67.72	0.45	24.05	1.55
Au/CeO₂-750	43.63	0.43	35.60	1.88

^a These values were determined by ICP.

Table S2. Reducibility of all the given catalysts obtained by H₂-TPR.

Samples	Peak position (T/°C)	H₂ consumption (umol.g_{cat}⁻¹)
CeO ₂	465.3	396
	716.5	353
Au/CeO ₂	95.5	926
	668.7	558
Au/CeO ₂ -350	89.3	632
	661.0	220
Au/CeO ₂ -550	149.5	470
	698.0	116
Au/CeO ₂ -750	172.5	247
	702.7	386

Table S3. Comparison of catalytic performance in HCHO oxidation over Au/CeO₂-550 and those catalysts reported in literature.

Catalysts	T (°C)	GHSV (h ⁻¹ or mL·g ⁻¹ ·h ⁻¹)	[HCHO] (ppm or mg·m ⁻³)	HCHO removal activity	Refs.
Au/CeO₂-550	21	36,000 mL·g ⁻¹ ·h ⁻¹	200 ppm	η = 100%	This work
Au/CeO₂	21	36,000 mL·g ⁻¹ ·h ⁻¹	200 ppm	η = 8%	This work
Au/CeO₂-350	21	36,000 mL·g ⁻¹ ·h ⁻¹	200 ppm	η = 13%	This work
Au/CeO₂-750	21	36,000 mL·g ⁻¹ ·h ⁻¹	200 ppm	η = 3%	This work
3% Au/CeO₂ (3DOM)	20	66,000 mL·g ⁻¹ ·h ⁻¹	8 ppm	η = 32%	⁹
3% Au/CeO₂-Co₃O₄ (3DOM)	20	66,000 mL·g ⁻¹ ·h ⁻¹	8 ppm	η = 70%	⁹
2.5% Au/FeO_x	24	30,000 mL·g ⁻¹ ·h ⁻¹	450 ppm	η = 33%	¹⁰
1% Au/γ-Al₂O₃	25	600,000 h ⁻¹	80 ppm	η = 73- 88%	¹¹
1% Au/SiO₂	25	600,000 mL·g ⁻¹ ·h ⁻¹	80 ppm	η = 35- 79%	¹²
1% Au/ HZSM-5 zeolite	25	600,000 mL·g ⁻¹ ·h ⁻¹	80 ppm	η = 19- 45%	¹²
7.1% Au/FeO_x	20	54,000 mL·g ⁻¹ ·h ⁻¹	6.25 mg·m ⁻³ ³	η = 20%	¹³
7.1% Au/FeO_x	40	54,000 mL·g ⁻¹ ·h ⁻¹	6.25 mg·m ⁻³ ³	η = 52%	¹³
1% Au/CeO₂	20	120,000 h ⁻¹	600 ppm	η = 79%	¹⁴
0.25% Au/α-MnO₂	70	60000 mL·g ⁻¹ ·h ⁻¹	500 ppm	η = 100%	¹⁵
1% Au/2D-Co₃O₄	25	55000 h ⁻¹	200 ppm	η = 50%	¹⁶
1% Au/ZrO₂-200	80	60000 mL·g ⁻¹ ·h ⁻¹	3000 ppm	η = 100%	¹⁷
3% Au-Pd/CeO₂	30	15,000 mL·g ⁻¹ ·h ⁻¹	8 ppm	η = 50%	¹⁸
0.25% Au/CeO₂	25	34,000 h ⁻¹	80 ppm	η = 41%	¹⁹
Au@SiO₂	100	15000 mL·g ⁻¹ ·h ⁻¹	500 ppm	η = 100%	²⁰
1.12Au/Ce₃Co	60		50 ppm	η = 100%	²¹
0.912Au/APTES@MCM-41	55	20000 mL·g ⁻¹ ·h ⁻¹	100 ppm	η = 100%	²²

Reference

1. Chiou, J. Y. Z.; Yang, S.-Y.; Lai, C.-L.; Kung, H.-Y.; Tang, C.-W.; Wang, C.-B., Steam Reforming of Ethanol over CoMg/SBA-15 Catalysts. *Modern Research in Catalysis* 2013, **02**, 13-21.
2. Gao, W.; Zhou, T.; Wang, Q., Controlled synthesis of MgO with diverse basic sites and its CO₂ capture mechanism under different adsorption conditions. *Chemical Engineering Journal* 2018, **336**, 710-720.
3. Li, H.; Li, L.; Chen, S.; Zhang, Y.; Li, G., Kinetic Control of Hexagonal Mg(OH)₂ Nanoflakes for Catalytic Application of Preferential CO Oxidation. *Chinese Journal of Chemistry* 2017, **35**, 903-910.
4. Delannoy, L.; Weiher, N.; Tsapatsaris, N.; Beesley, A. M.; Nchari, L.; Schroeder, S. L. M.; Louis, C., Reducibility of supported gold (III) precursors: influence of the metal oxide support and consequences for CO oxidation activity. *Topics in Catalysis* 2007, **44**, 263-273.
5. Chen, S.; Luo, L.; Jiang, Z.; Huang, W., Size-Dependent Reaction Pathways of Low-Temperature CO Oxidation on Au/CeO₂ Catalysts. *ACS Catalysis* 2015, **5**, 1653-1662.
6. Jin, Z.; Song, Y.-Y.; Fu, X.-P.; Song, Q.-S.; Jia, C.-J., Nanoceria Supported Gold Catalysts for CO Oxidation. *Chinese Journal of Chemistry* 2018, **36**, 639-643.
7. Aguirre, A.; Barrios, C. E.; Aguilar-Tapia, A.; Zanella, R.; Baltanás, M. A.; Collins, S. E., In-Situ DRIFT Study of Au-Ir/Ceria Catalysts: Activity and Stability for CO Oxidation. *Topics in Catalysis* 2015, **59**, 347-356.
8. Huang, X.-S.; Sun, H.; Wang, L.-C.; Liu, Y.-M.; Fan, K.-N.; Cao, Y., Morphology effects of nanoscale ceria on the activity of Au/CeO₂ catalysts for low-temperature CO oxidation. *Applied Catalysis B: Environmental* 2009, **90**, 224-232.
9. Liu, B.; Liu, Y.; Li, C.; Hu, W.; Jing, P.; Wang, Q.; Zhang, J., Three-dimensionally ordered macroporous Au/CeO₂-Co₃O₄ catalysts with nanoporous walls for enhanced catalytic oxidation of formaldehyde. *Applied Catalysis B: Environmental* 2012, **127**, 47-58.
10. Tang, Z.; Zhang, W.; Li, Y.; Huang, Z.; Guo, H.; Wu, F.; Li, J., Gold catalysts supported on nanosized iron oxide for low-temperature oxidation of carbon monoxide and formaldehyde. *Applied Surface Science* 2016, **364**, 75-80.
11. Chen, B.; Zhu, X.; Wang, Y.; Yu, L.; Shi, C., Gold stabilized on various oxide supports catalyzing formaldehyde oxidation at room temperature. *Chinese Journal of Catalysis* 2016, **37**, 1729-1737.
12. Chen, B.-B.; Zhu, X.-B.; Wang, Y.-D.; Yu, L.-M.; Lu, J.-Q.; Shi, C., Nano-sized gold particles dispersed on HZSM-5 and SiO₂ substrates for catalytic oxidation of HCHO. *Catalysis Today* 2017, **281**, 512-519.
13. Li, C.; Shen, Y.; Jia, M.; Sheng, S.; Adebajo, M. O.; Zhu, H., Catalytic combustion of formaldehyde on gold/iron-oxide catalysts. *Catalysis Communications* 2008, **9**, 355-361.
14. Li, G.; Li, L., Highly efficient formaldehyde elimination over meso-structured M/CeO₂ (M = Pd, Pt, Au and Ag) catalyst under ambient conditions. *RSC Advances* 2015, **5**, 36428-36433.
15. Chen, J.; Yan, D.; Xu, Z.; Chen, X.; Chen, X.; Xu, W.; Jia, H.; Chen, J., A Novel Redox Precipitation to Synthesize Au-Doped alpha-MnO₂ with High Dispersion toward Low-Temperature Oxidation of Formaldehyde. *Environmental science & technology* 2018, **52**, 4728-

4737.

16. Ma, C.; Wang, D.; Xue, W.; Dou, B.; Wang, H.; Hao, Z., Investigation of formaldehyde oxidation over $\text{Co}_3\text{O}_4\text{-CeO}_2$ and $\text{Au/Co}_3\text{O}_4\text{-CeO}_2$ catalysts at room temperature: effective removal and determination of reaction mechanism. *Environmental science & technology* 2011, **45**, 3628-34.
17. Hong, Y.-C.; Sun, K.-Q.; Han, K.-H.; Liu, G.; Xu, B.-Q., Comparison of catalytic combustion of carbon monoxide and formaldehyde over Au/ZrO_2 catalysts. *Catalysis Today* 2010, **158**, 415-422.
18. Wang, Q.; Jia, W.; Liu, B.; Zhao, W.; Li, C.; Zhang, J.; Xu, G., Controllable synthesis of nearly monodisperse spherical aggregates of CeO_2 nanocrystals and their catalytic activity for HCHO oxidation. *Chemistry, an Asian journal* 2012, **7**, 2258-67.
19. Chen, B.-b.; Zhu, X.-b.; Crocker, M.; Wang, Y.; Shi, C., Complete oxidation of formaldehyde at ambient temperature over $\gamma\text{-Al}_2\text{O}_3$ supported Au catalyst. *Catalysis Communications* 2013, **42**, 93-97.
20. Chen, D.; Shi, J.; Shen, H., High-dispersed catalysts of core-shell structured Au@SiO_2 for formaldehyde catalytic oxidation. *Chemical Engineering Journal* 2020, **385**, 123887.
21. Qu, J.; Chen, D.; Li, N.; Xu, Q.; Li, H.; He, J.; Lu, J., 3D Gold-Modified Cerium and Cobalt Oxide Catalyst on a Graphene Aerogel for Highly Efficient Catalytic Formaldehyde Oxidation. *Small* 2019, **15**, e1804415.
22. Xu, J.; Qu, Z.; Wang, Y.; Huang, B., HCHO oxidation over highly dispersed Au nanoparticles supported on mesoporous silica with superior activity and stability. *Catalysis Today* 2019, **327**, 210-219.